Journal Pre-proofs

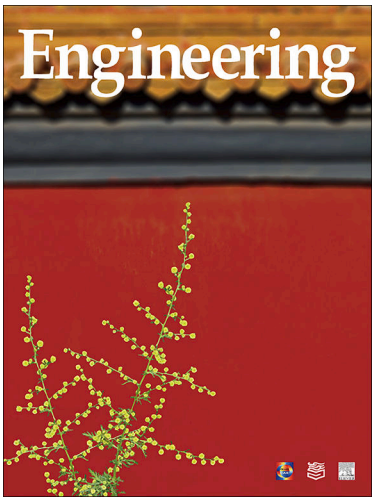

Article

A General Model for Predicting Machining Deformation Fields in Structural Components with Varying Geometries Using a Geometry-Oriented Neural Operator

Zhiwei Zhao, Changqing Liu, Yan Jin, Yifan Zhang, Yingguang Li

PII: S2095-8099(25)00554-5
DOI: https://doi.org/10.1016/j.eng.2025.08.036
Reference: ENG 2053

To appear in: *Engineering*

Received Date: 20 November 2024
Revised Date: 4 March 2025
Accepted Date: 1 August 2025

Please cite this article as: Z. Zhao, C. Liu, Y. Jin, Y. Zhang, Y. Li, A General Model for Predicting Machining Deformation Fields in Structural Components with Varying Geometries Using a Geometry-Oriented Neural Operator, *Engineering* (2025), doi: https://doi.org/10.1016/j.eng.2025.08.036

Intelligent Manufacturing—Article

A General Model for Predicting Machining Deformation Fields in Structural Components with Varying Geometries Using a Geometry-Oriented Neural Operator

Zhiwei Zhao [a,b], Changqing Liu [a], Yan Jin [b], Yifan Zhang [a], Yingguang Li [a,*]

[a] *College of Mechanical and Electrical Engineering, Nanjing University of Aeronautics and Astronautics, Nanjing, 210016, China*

[b] *School of Mechanical and Aerospace Engineering, Queen's University Belfast, Belfast BT9 5AH, UK*

* Corresponding author.

E-mail address: liyingguang@nuaa.edu.cn (Y. Li)

Abstract: Controlling machining deformations resulting from unbalanced stress fields inside structural components is a significant challenge in the manufacturing industry. Prediction of machining deformation fields is fundamental for deformation control and requires numerous iterations to optimize the machining process. Conventional prediction methods such as numerical analysis are tailored to a fixed geometry, making them time-consuming and inefficient for components with various geometries. In this study, a general data-driven model is proposed for predicting machining deformation fields in components with varying geometries and stress fields. This model is based on a geometry-oriented neural operator that incorporates global geometry information into the function space, modeling the relationship between the input function (stress fields) and the output function (deformation fields). Global geometric information is extracted using a graph neural network applied to a geometric graph and embedded into the input and output function space through an encoder-query framework. The proposed model achieved low root-mean-squared errors ranging from 0.001 to 0.016 mm, with maximum prediction errors between 0.003and 0.047 mm across different types of components, including beams and frames. The main contribution of this research is the significant advancement in the application of neural operators to the development of general models for predicting machining deformation. The underlying principles of the proposed model provide an important reference for wider applications related to the control of machining deformation in the context of digital and intelligent manufacturing.

Keywords: Structural components; Machining deformation field prediction; General model; Neural operator

1. Introduction

Machining deformation of components during manufacturing is a primary problem in quality control, particularly for machining large-scale structural components, such as those used in aircraft and high-value equipment. These components, which are characterized by complex geometries and large dimensions, are highly susceptible to deformation after machining operations, which can significantly affect the assembly precision, fatigue life, and overall performance [1]. Deformation during machining not only compromises quality but also incurs substantial costs, making it a longstanding challenge. To address this challenge, deformation-prediction models have been increasingly integrated into process planning to minimize trial-and-error procedures, scrap, and production costs [2]. However, controlling machining deformation requires extensive iterative optimization, often involving multiple time-consuming deformation predictions to refine the control process. Thus, accurate and rapid deformation prediction is essential for effective deformation control [3]. The primary cause of machining deformation is the disturbance of the residual stress field within the material [4] that occurs during the material removal process. This disturbance can lead to an overall component deformation (global type) and deformation in specific areas or features of the component (local type). Therefore, developing efficient and accurate methods for deformation field prediction is crucial for controlling both global and local deformation types, which remains highly challenging owing to complex and varying component geometries and stress fields.

The prediction of deformation fields involves solving for the deformation field caused by the respective unbalanced stress fields within a component, which is achieved by solving partial differential equations (PDEs). Existing methods for deformation-field prediction can be broadly categorized into conventional numerical computation and data-driven

methods. Numerical computation methods, such as the finite element method (FEM), discretize complex geometries i[illegible]on of complex geometries with various initial and boundary conditions, making it suitable for large-scale components. Numerous studies [5–7] have established the critical role of residual stress in predicting the deformation of aerospace components. However, in real-life manufacturing, the component geometry changes continuously during machining, requiring frequent recalculations; thus, the computational efficiency is significantly low. To address this problem, some studies have focused on accommodating geometric changes caused by the continuous machining process through strategies such as birth-death elements, mesh redefinition [8] and adaptation [9], which enhance both computational efficiency and prediction accuracy. However, for large and complex components, many elements require significant data memory, computational power, and processing time [10]. In addition, prediction models based on numerical methods are typically specialized models, in which any changes in the geometry or stress field of a component require a complete recalculation, further reducing the efficiency of deformation field prediction.

Recently, data-driven methods have been widely applied for solving PDEs. Among these, the physics-informed neural network (PINN) method approximates solution functions using neural networks and functions as a mesh-free method [11]. PINNs are well-suited for problems with clear physical laws that fall short in terms of accuracy and efficiency when applied to predicting deformation fields within components of complex geometry. Additionally, PINNs require retraining of the neural network whenever there are changes in the geometry or parameter [12], which constrains the effectiveness of the deformation prediction when dealing with complex and varying conditions. Furthermore, the methods based on deep learning, which demonstrate strong fitting capabilities and possess a certain level of generalization after training, are suitable for constructing deformation-prediction models. Liu et al. [13] developed a deformation prediction model based on a neural network trained using data from an FEM that captured the relationship between machining parameters and distortions. Rodriguez-Sanchez et al. [14] combined artificial neural networks with FEM to model deformation and provided a reliable indication of localized distortion patterns. However, these models are typically defined based on a single geometry. For varying geometries, Zhao et al. [15] employed height maps to represent the geometry and neural networks to map the relationship between a geometry-process tensor and the resulting deformation. To address more complex geometries, Zhao et al. [16] further proposed diffeomorphic mapping methods to map geometric surfaces onto a common input domain as geometric images, and proposed a neural network framework for predicting subsequent machining deformation using monitored deformation forces. Although these methods can predict the deformation fields for different geometries, they can only establish mappings between discrete numerical domains, limiting their ability to predict deformation at specific selected points rather than predicting the complete representation of a deformation field.

Recently, neural operators have emerged as a promising research focus for solving PDEs [17]. Neural operators utilize neural networks to learn function-to-function mapping from the parameter functions of PDEs to their solution functions, making them well-suited for modeling the relationships between stress and deformation fields within components. By leveraging neural operators, the computation of PDEs can be accelerated by several orders of magnitude compared to conventional numerical methods. This advancement has shown significant importance in structural design and process optimization. Notable neural operators include the Deep Operator Network (DeepONet) [18] and the Fourier Neural Operator (FNO) [19], with many further advancements in this field [20–23]. However, these methods are still primarily defined with respect to fixed geometric domains, and thus require retraining when the component geometry changes. This limitation poses a significant challenge for predicting deformations in components with varying geometries during machining, because the need for multiple operator models may lead to substantial time and data processing costs, thereby reducing the efficiency and practicality of predicting the deformation of complex structural components. This leads to our central research question: whether a single neural operator framework can generalize across geometries and stress fields without retraining, enabling efficient and accurate deformation field prediction for a wide variety of structural components. In terms of neural operators for varying geometry domains, there are fundamental difficulties in representing the geometry domain. Few studies have been conducted using techniques such as parameterized geometry representations [24], level set functions [25], geometric gating mechanisms [26], and mapping onto a latent domain [27] or a common reference domain [28,29]. However, these methods have limitations in predicting the deformation fields of complex structural components. They can only handle simple geometries, two-dimensional (2D) geometries, and geometries of similar shapes, and lack theoretical guarantees.

In summary, both numerical and data-driven methods for solving PDEs are based on specialized models defined with respect to specific conditions, including fixed geometries and parameters, such as the FEM and PINNs. Additionally, models are defined with respect to fixed geometries but varying parameter functions, as seen in some neural operators. However, there is an urgent need for general models capable of rapidly solving deformation fields within components with varying geometric domains and stress fields. In this study, we propose a general model, referred to as the geometry-oriented neural operator (GONO), for predicting deformation fields within components with varying geometries and stress fields. This model is not only applicable to varying stress fields, but also adaptable to changing geometric domains. The proposed method was experimentally validated using various components, including frames and beams of different sizes and structures. The root mean squared errors of the prediction were within 0.016 mm, with the maximum absolute

methods, satisfying the strict requirements for guiding the process optimization of deformation control.

2. Proposed GONO for predicting machining deformation fields

In this section, we define the problem setting for predicting machining deformation fields and introduce the proposed GONO framework.

2.1. Problem formulation

Let domain $D \subset \mathbb{R}^3$ represent the geometry of a component, where D varies across different parts and $\mathbb{R}$ denotes the set of real numbers. These geometries may include complex features such as pockets, ribs, and varying thicknesses. Domain $\mathbb{D}$ is denoted by D_s with geometry parameter $s \in S$, where s is a part-level parameter and S denotes the parameter set with $S \subset \mathbb{R}^s$, the s-dimensional parameter space used to parameterize domain D.

The deformation and stress fields over $\mathbb{D}$ can be considered as functions defined on D: $u(x)$ and $f(x)$, respectively. The objective is to predict the deformation field $u(x)$ using the stress field $f(x)$. Given this setup, let L denotes a partial differential operator that describes the relationship between the stress field and resulting deformation field.

$$\begin{aligned} L(u) &= f, \text{in } D_s \\ u &= b \end{aligned} \qquad (1)$$

where $f(x) \in \mathbb{F}$, $u(x) \in U$, and $b(x) \in B$. $b(x)$ denotes a boundary condition defined on δD_s. We assume that S, $\mathbb{F}$, B, and U are the Banach spaces with a given norm. We define the mapping φ from the stress fields to the deformation field as

$$\varphi: S \times B \times F \rightarrow U \qquad (2)$$

This formulation allows the prediction of deformation fields across varying geometries and stress conditions, offering a flexible and efficient solution to the problem of machining deformation field prediction.

2.2. Framework of GONO

The proposed GONO framework leverages a combination of graph neural network (GNN) and neural operator architectures to effectively embed geometry information and model the operator φ, as shown in Fig. 1. The extraction of geometric information is crucial for predicting the deformation field. In this method, complex and varying geometries are represented using geometric graphs and are processed using a GNN to extract global low-dimensional geometric information. This encoded information is integrated into an encoder-query structure to construct an operator capable of predicting the deformation fields.

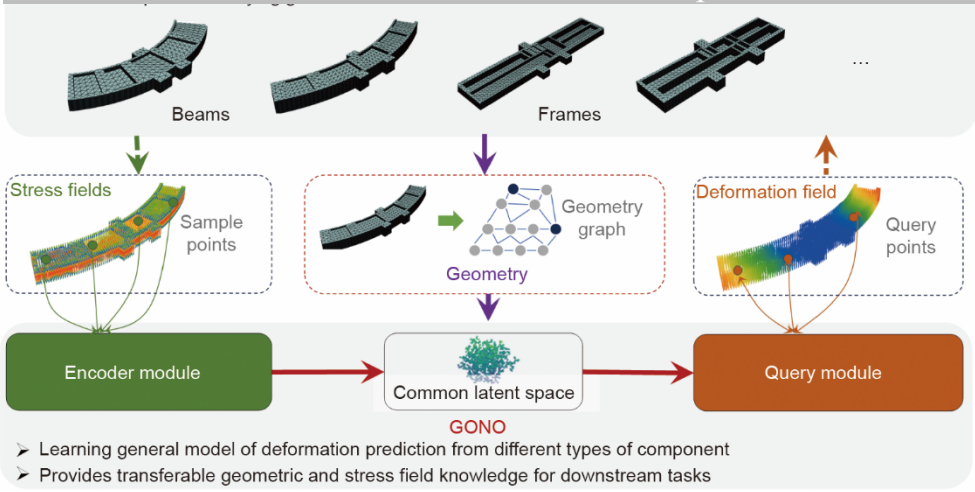

Fig. 1. Framework of GONO: the model predicts machining deformation for components with varying geometries and stress fields. The geometry module represents the component as a geometry graph and, together with the encoder module, encodes stress and geometric information into a common latent space. The query module then predicts the deformation field at query points.

2.2.1. Geometry information embedding based on geometry graph and GNNs

Components are typically represented as solid objects, making it crucial to efficiently capture and express their geometric characteristics. To achieve this, the surface of the component, denoted as S_D, is extracted, represented by a geometric graph, and mapped into a latent space, where the geometry is compactly represented by a set of latent variables $\boldsymbol{g}$, as illustrated in Fig. 2(a). These latent variables $\boldsymbol{g}$ provide a concise and efficient representation of the geometry, allowing the model to effectively handle a wide variety of geometric configurations.

First, the surface S_D is represented as a mesh, which is a geometric graph $G = (V, E)$, with a set of nodes V, edges E and their corresponding features. The features of each node $v \in \mathbb{R}^3$ represent the geometric attributes of the corresponding points on the surface, specifically their coordinates $v = (x_v, y_v, z_v)$. The edges E in the graph represent the connectivity between these nodes without additional feature attributes.

To extract meaningful global geometric information of the components from the geometry graph G, a GNN is employed that propagates messages of node attributes across the edges, effectively capturing the relationships between different parts of the geometry. Let $\boldsymbol{h}_v^{(l)}$ represent the feature vector of node v in layer l. The feature update process in the GNN can be described as follows.

$$\boldsymbol{m}_v^{(l+1)} = \sum_{v' \in V(v)} \phi\left(\boldsymbol{h}_v^{(l)}, \boldsymbol{h}_{v'}^{(l)}, e_{vv'}\right), \qquad (3)$$

where $\boldsymbol{m}_v^{(l+1)}$ is the message received by node v in layer $l+1$, $\boldsymbol{h}_{v'}^{(l)}$ is the feature of the neighboring node v', and $e_{vv'}$ is the edge feature between nodes v and v'. Function ϕ is a typical neural network. After the message passing, the node features are updated using an update function ψ, which incorporates the aggregated messages:

$$\boldsymbol{h}_v^{(l+1)} = \psi\left(\boldsymbol{h}_v^{(l)}, \boldsymbol{m}_v^{(l+1)}\right), \qquad (4)$$

where ψ denotes another neural network. This update rule allows each node to iteratively refine its feature representation by incorporating information from its neighbors. After several layers of feature aggregation and updating, a global pooling operation, such as max pooling, is applied across all nodes in the graph to extract a global geometric embedding $\boldsymbol{g}$

$$\boldsymbol{g} = \text{MaxPool}\left(\boldsymbol{h}_v^{(L)} | v \in V\right) \quad (5)$$

where L denotes the total number of GNN layers and MaxPool is a pooling operator that takes the element-wise maximum over the node embeddings. This operation effectively condenses the geometric information of the component into a compact latent representation $\boldsymbol{g}$. This operation effectively summarizes the geometric information of the entire surface into a set of latent variables $\boldsymbol{g}$, which capture the essential global geometric characteristics of the component.

2.2.2. Neural operator architecture

This section describes the architecture of the neural operator. Here, both the input and output functions are discretized into a series of points, which leverages the fact that in practical applications, both the input and output functions are often sampled at discrete locations.

The input function $\mathrm{f(x)}$, such as, the stress field, is sampled at n discrete points $(x_1, x_2, ..., x_n)$, where $x \in D$ represents the spatial coordinates within the domain D, resulting in a set of values $(f(x_1), f(x_2), ..., f(x_n)) = (\sigma_1, \sigma_2, ..., \sigma_n)$ with residual stress $\sigma_i = f(x_i)$ for $i = 1, ..., n$. Similarly, the output function representing the deformation field $u(x)$, is also sampled at a set of discrete points within the domain, represented by $(d_1, d_2, ..., d_m)$.

In this study, an operator is constructed as an approximation out of two maps:

$$\varphi \approx O \circ P \quad (6)$$

where the first map, denoted as P, projects the input function onto a finite-dimensional manifold, encapsulating the global features of the stress fields. The second map O approximates the operator and constructs the output function, which corresponds to the deformation fields. "∘" represents a composition of mappings in the neural operator framework, which indicates that O operates on the output of P, forming a two-step mapping from input to output functions.

The first map P is obtained by applying an encoder neural network module to the set of input data points. Specifically, for each point x_i, the neural network maps the input value $f(\mathrm{x}_i)$ along with the corresponding spatial coordinates x_i and geometric information to a latent variable $\boldsymbol{k}_i$ as follows:

$$\boldsymbol{k}_i = P(x_i, f(x_i), \boldsymbol{g}), \quad (7)$$

The latent variables $(\boldsymbol{k}_1, \boldsymbol{k}_2, ..., \boldsymbol{k}_n)$ are aggregated to form a global representation $\boldsymbol{k}_f$ of the input function.

$$\boldsymbol{k}_f = \text{Aggregate}(\boldsymbol{k}_1, \boldsymbol{k}_2, ..., \boldsymbol{k}_n). \quad (8)$$

where the aggregation function is a sum, mean, or max pooling operation. Here, a mean function is applied. This global representation $\boldsymbol{k}_f$ captures the essential information of the input function across the entire domain, which can be deemed a common space for all fields defined on various geometries.

The second map O is realized through a query neural network module, which approximates the operator by constructing the output function $u(x)$. For each output point x_j, the map O uses the global input representation $\boldsymbol{k}_f$ and the coordinates of the query point x_j, together with the geometric information $\boldsymbol{g}$, to predict the corresponding deformation value $u(x_j)$:

$$u(x_j) = \mathrm{O}\left(x_j, \boldsymbol{k}_f, \boldsymbol{g}\right), \quad (8)$$

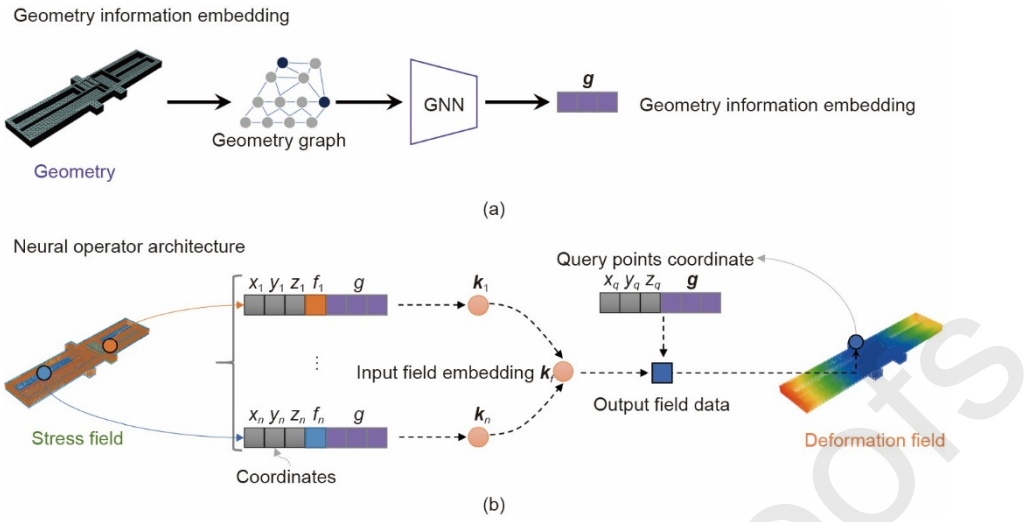

Fig. 2. Details of the GONO architecture: (a) Geometry information embedding module first represents the component's geometry as a geometry graph and embeds geometry as geometry information $\boldsymbol{g}$. (b) Neural operator architecture is used for mapping the stress field to the deformation field. The stress field is sampled at specific points (x_i,y_i,z_i) and encoded along with geometric information $\boldsymbol{g}$ to obtain latent variables $\boldsymbol{k}_i$. The latent variables $(\boldsymbol{k}_i,...,\boldsymbol{k}_n)$ of all points are then aggregated to form a global latent representation $\boldsymbol{k}_f$ of the input field. This representation $\boldsymbol{k}_f$ is subsequently used to predict the deformation field at query points (x_q,y_q,z_q).

The loss function used for training the neural operator is based on the L_2 relative loss, which measures the difference between the predicted and true deformation fields. Given a set of N training samples, each with a true deformation field u^i_{true} and predicted deformation field $\mathrm{u}^{\mathrm{i}}_{\text{pred}}$, the overall loss function is defined as follows:

$$\text{Loss} = \sum_{\mathrm{t}=1}^{N} \frac{\| u^{\mathrm{t}}_{\text{pred}} - u^{\mathrm{t}}_{\text{true}} \|_2}{\| u^{\mathrm{t}}_{\text{true}} \|_2} \qquad (8)$$

where $\|\cdot\|_2$ denotes the L_2 norm, $u^{\mathrm{t}}_{\text{pred}} = (u^{\mathrm{t}}_{\text{pred}}(x_1),...,u^{\mathrm{t}}_{\text{pred}}(x_m))$ and $u^{\mathrm{t}}_{\text{true}} = (u^{\mathrm{t}}_{\text{true}}(x_1),...,u^{\mathrm{t}}_{\text{true}}(x_m))$ represents the predicted and ground true deformation field values for the t training sample at query points $(x_1,...,x_m)$, respectively.

In summary, the neural operator architecture is composed of two primary maps: the first map P transforms the discretized input function into a global latent representation, whereas the second map O approximates the deformation field as a function of the global latent variable and spatial coordinates, as shown in Fig. 2(b). This architecture enables the efficient and scalable prediction of deformation fields by leveraging the ability of neural networks to handle high-dimensional and complex functions across varying geometric configurations.

3. Experiment and results

3.1. Dataset implementation details

Experiments were conducted on two typical structural components commonly used in aircraft manufacturing: rectangular frames and C-shaped beams. Both components were manufactured by removing the pocket feature materials using machining processes. The components materials were subjected to various stress fields with different distributions and magnitudes, primarily considering in-plane stress fields, σ_x and σ_y.

For the geometry generation process, rectangular frames with varying lengths, widths, and thicknesses were designed with different numbers, sizes, and depths of pocket features on the top plane of the components, as shown in Fig. 3(a). The C-shaped beams were designed with varying radius, widths, thicknesses, and covering angles. The pockets on the

stress field variables for rectangular frames and C-shaped beams are shown in Table 1.

Table 1. Levels of geometric and stress field variables for rectangular frames and C-shaped beams.

Component type	Length (mm)	Radius (mm)	Width (mm)	Thickness (T) (mm)	Beam angle (°)	Number of pockets	Pocket depth (mm)	Stress field range (MPa)
Rectangular frame	200–600	N/A	60–180	20–40	NA	3–10	2–(T − 2)	±100
C-shaped beam	NA	200–600	40–80	20–40	40–80	6–10	2–(T − 2)	±100

NA: not available.

The stress fields inside both the rectangular frames and C-shaped beams were based on the typical residual stress distribution observed in aluminum alloy components, characterized by an "M-shaped" profile along the depth direction. The M-shaped distribution was controlled using a varying polynomial function. The magnitude of the stress field varied within ±100 MPa. This distribution and variation in the geometry and stress fields provided a comprehensive dataset for evaluating the performance of the proposed neural operator across different types of structural components under varying stress conditions.

To generate the required data, finite element simulations were conducted on the generated geometries to obtain datasets of the deformation forces and displacements. The components were constrained using three locating pads, as shown in Fig. 3. These locating pads were added to the central region of each component to provide fixed boundary conditions and ensure a consistent reference for the deformation fields. Each pad measured 30 mm × 30 mm, and the distances between the two pads varied randomly within the range of 80–120 mm. This was the only boundary condition that allowed the resulting deformation fields to serve as a baseline for easy comparison.

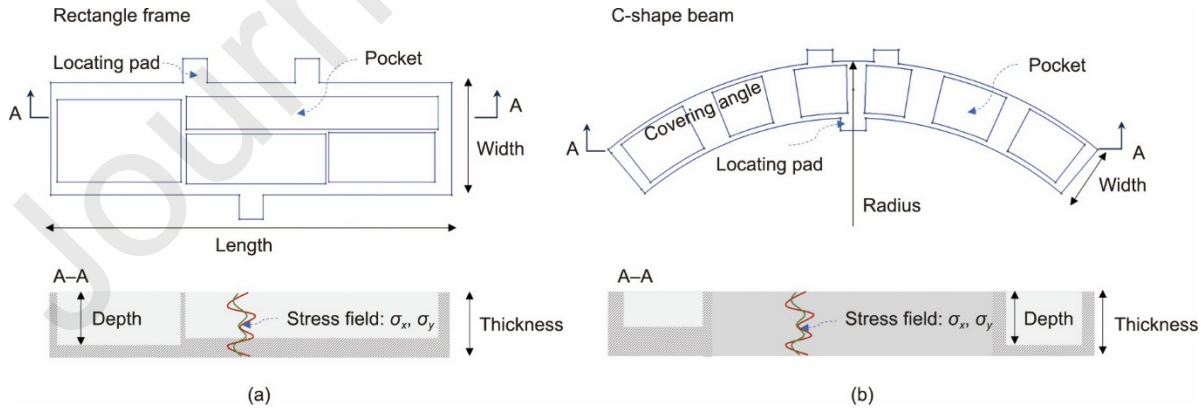

Fig. 3. Details of the generation process for the components deformation dataset. (a) The rectangular frame generation process, where geometric variables include the number, position, and depth of pockets, as well as the length, width, and height of the frame. (b) The C-shaped beam generation process, where geometric variables include the number, position, and depth of pockets, along with the radius, width, thickness, and covering angle of the beam.

The mesh size used for the simulations was set to 1 mm to capture the effects of the stress field. This fine mesh enables a more detailed representation of the stress distribution and its impact on the deformation of the components. A total of 700 components were simulated, encompassing various combinations of stress fields, geometries, and the resulting deformation fields.

In this section, we present the results of the experiments conducted to evaluate the performance of the proposed GONO framework in predicting machining deformation fields. The results were analyzed based on several criteria, including the prediction accuracy, computational efficiency, and application across parts with series-machined geometry. A comparative analysis with conventional numerical methods is provided to demonstrate the advantages of the proposed approach.

3.2.1. Machining deformation prediction in sequence machine process

The model was trained on a dataset consisting of both the frame and C-shaped beam components. Training was performed at a learning rate of 0.0001, batch size of 8 and 1500 training epochs using an NVIDIA A100 GPU (NVIDIA Corporation, USA). Typical frame and beam structures were selected to validate the ability of the trained model to predict deformation during the sequence machining process of structural components. A layer-by-layer removal method was simulated, in which the material was removed in nine processes, each removing 2 mm of material from the top. The trained model was then used to predict the deformation fields of the components at different stages of the process.

The results for the frame parts are shown in Fig. 4, which presents the geometries, label deformations, predicted deformations, and deformation predicted error for process 1 and process 9. The observed differences between the predicted and actual deformation fields are minimal and within a narrow range, demonstrating that the model achieves a high level of prediction accuracy.

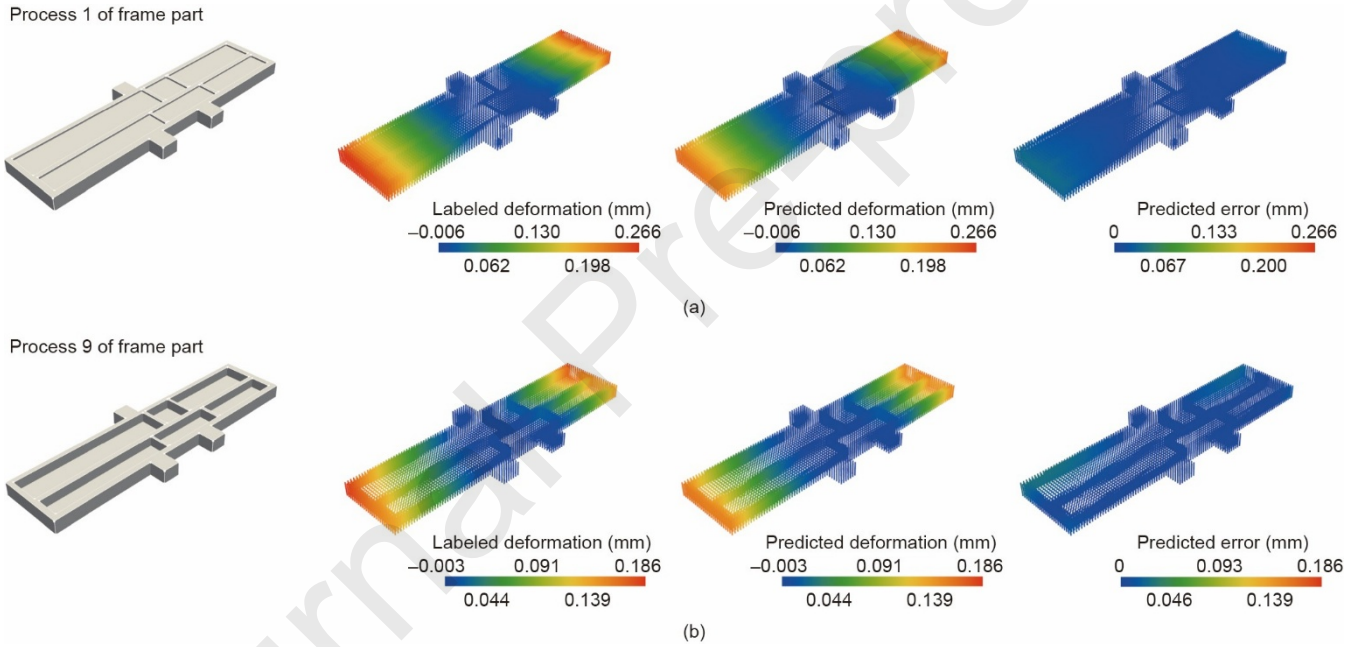

Fig. 4. Deformation prediction results for a frame part during different machining processes. (a) Process 1: the initial machining process, showing the labeled deformation, predicted deformation, and predicted error distribution. (b) Process 9: the final machining process after multiple material removal steps, with corresponding labeled deformation, predicted deformation, and predicted error.

The results for the C-shaped beam parts are shown in Fig. 5, where the geometry of the beam after the removal of each layer, the predicted deformation field, and deformation difference are displayed for process 1 and process 9. Similar to the results observed for the frame parts, the model predictions demonstrated a high level of accuracy across all processes. Supplement S1 in Appendix A provides additional details of the prediction results in the sequence machine process.

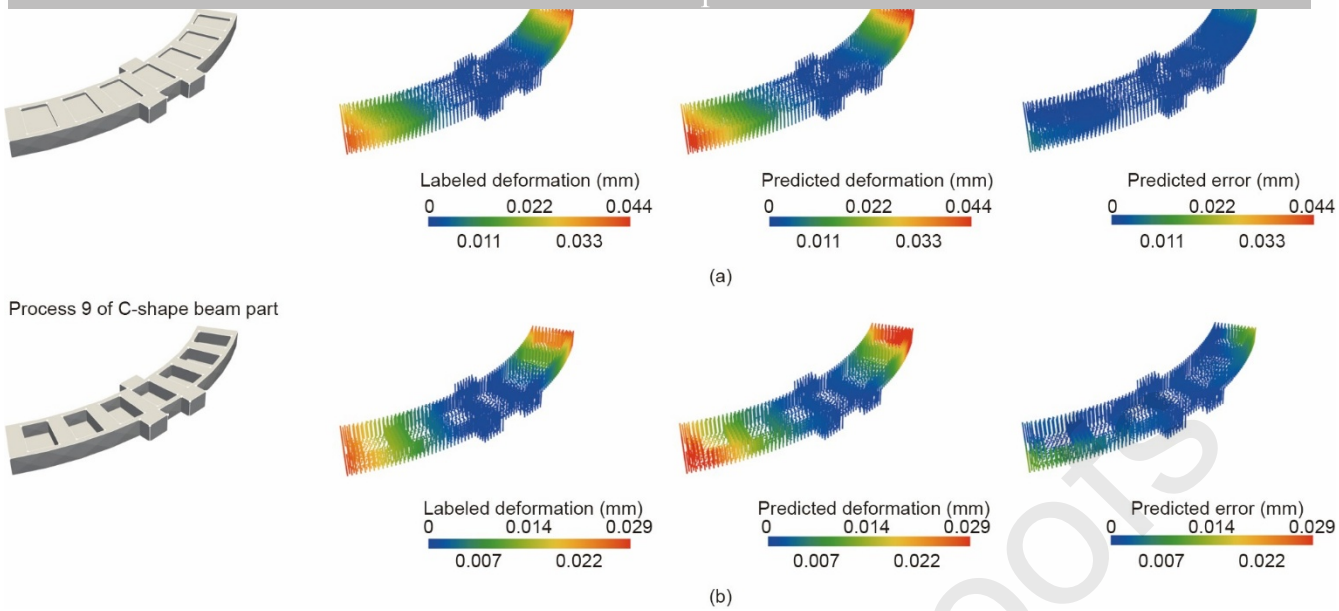

Fig. 5. Deformation prediction results for a C-shaped beam part during different machining processes. (a) Process 1: the initial machining stage, showing the labeled deformation, predicted deformation, and predicted error distribution. (b) Process 9: the final machining stage showing the labeled deformation, predicted deformation, and predicted error distribution.

Based on the obtained deformation fields, the surface deformations at $Z = 0$ (Z is coordinate along the thickness direction) for the frame and beam components were extracted, as shown in Fig. 6. The predicted deformation fields (Figs. 6(b) and (d)) closely matched the labeled deformation fields (Figs. 6(a) and (c)) for both the frame and beam components. This indicates that the proposed model effectively captured the overall deformation patterns.

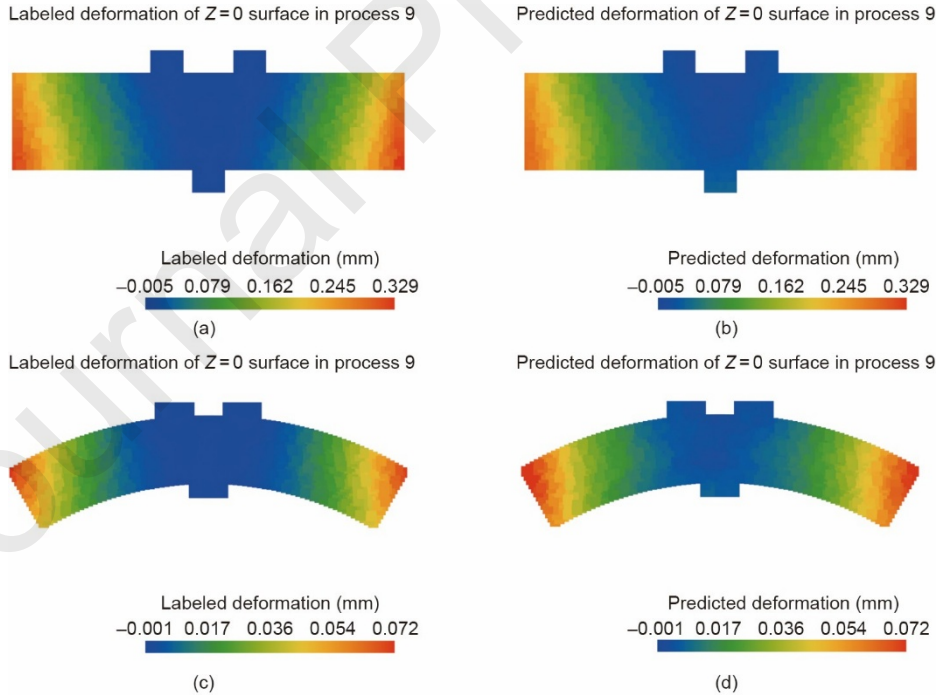

Fig. 6. Surface deformation at $Z = 0$ for the frame and C-shaped beam components. (a) Labeled deformation of the rectangular frame at $Z = 0$. (b) Predicted deformation of the rectangular frame at $Z = 0$. (c) Labeled deformation of the C-shaped beam at $Z = 0$. (d) Predicted deformation of the C-shaped beam at $Z = 0$.

Further analysis was conducted by selecting six points along the length of both the frame and C-shaped beam components and tracking their deformation throughout the machining process, as shown in Figs. 7 and 8. The predicted deformation (red line) closely followed the labeled deformation (blue dashed line) at both selected points across all

machining steps. The results proved that the model could capture local deformation patterns even in components with

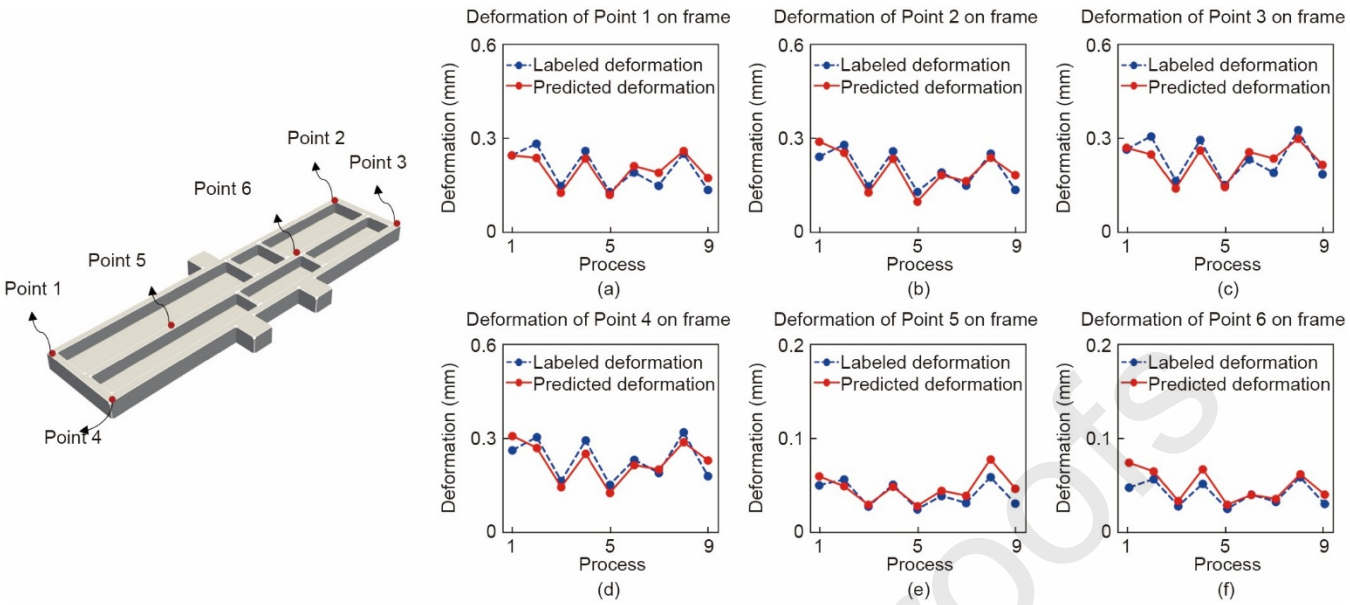

Fig. 7. Deformation variations from (a–f) Point 1 to Point 6 along the length of the frame.

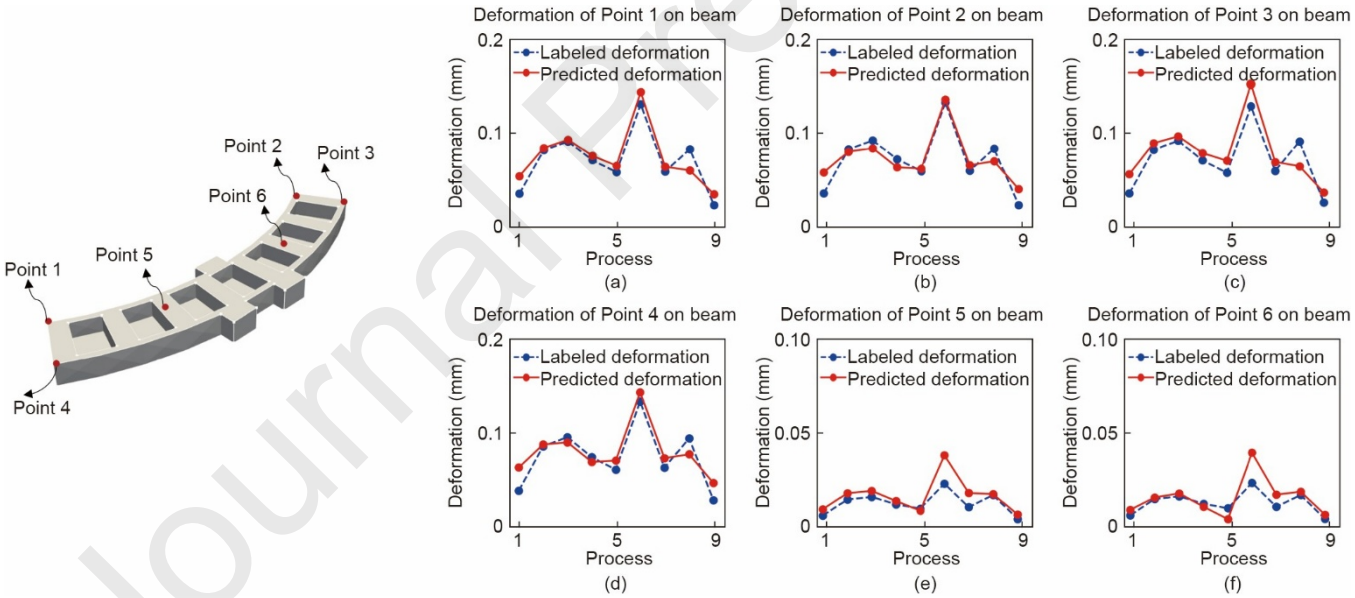

Fig. 8. Deformation variations from (a–f) Point 1 to Point 6 along the length of the C-shape beam.

3.2.2 Machining deformation prediction in different types of components

To further validate the ability of the model to predict deformation fields under different stress fields and geometries, tests were conducted on separate datasets for 10 frames and 10 beam parts. The prediction results are shown in Figs. 9 and 10. Fig. 9 illustrates the deformation predictions for two different frame components with significantly different geometries and stress fields. The results showed that the model demonstrated high accuracy in predicting deformation across these diverse conditions. For both frame parts, the predicted deformation fields closely matched the labeled deformations. This indicates that the model effectively captures the deformation behavior even under varying geometric configurations and stress conditions.

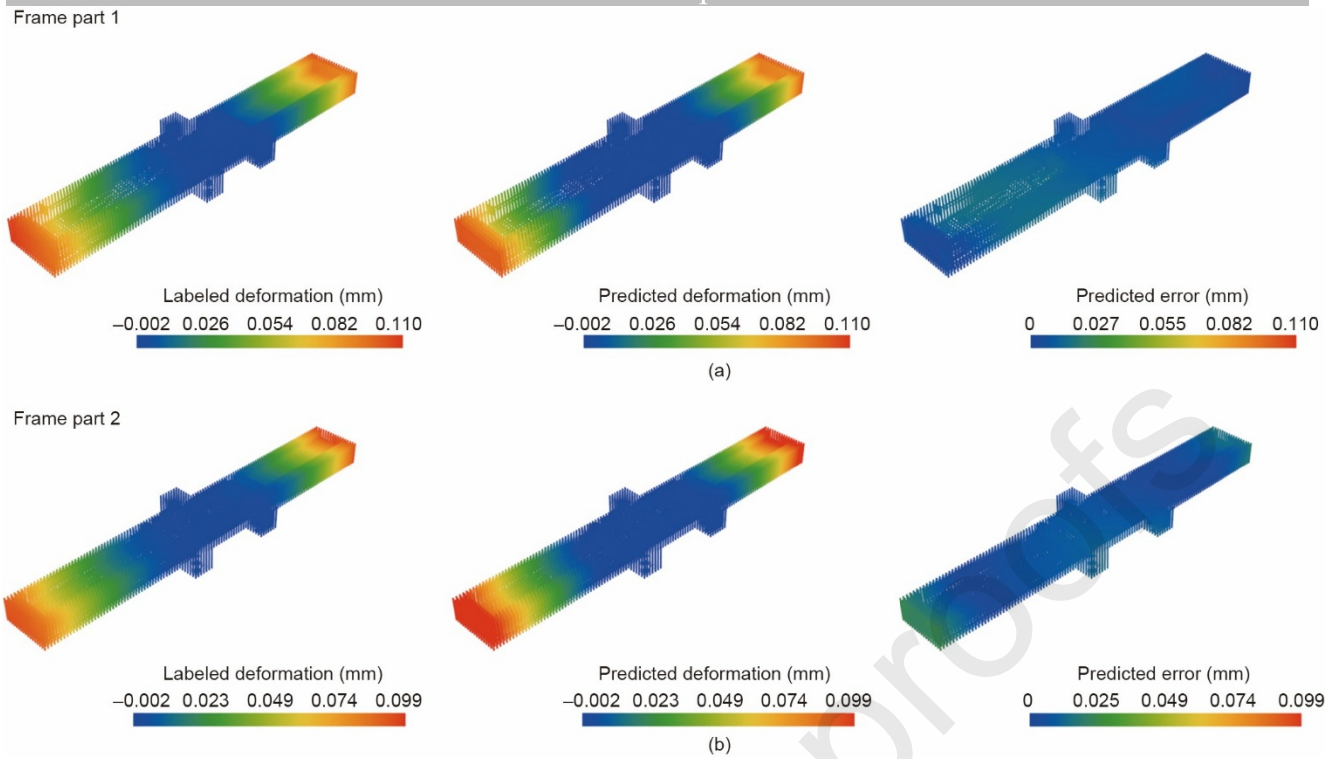

Fig. 9. Predicted deformation results for two different frame parts under varying stress fields and geometries. (a) Frame part 1: comparison of labeled deformation, predicted deformation, and predicted error. (b) Frame part 2: comparison of labeled deformation, predicted deformation, and predicted error.

Fig. 10 shows the results for two different C-shaped beam parts that exhibit distinct geometric and stress characteristics similar to the frame parts. The predictions for the C-shaped beam part 1 and part 2 show that the model maintained a high level of accuracy across all scenarios. This further confirms the robustness of the model in dealing with different geometries and stress distributions for different component types.

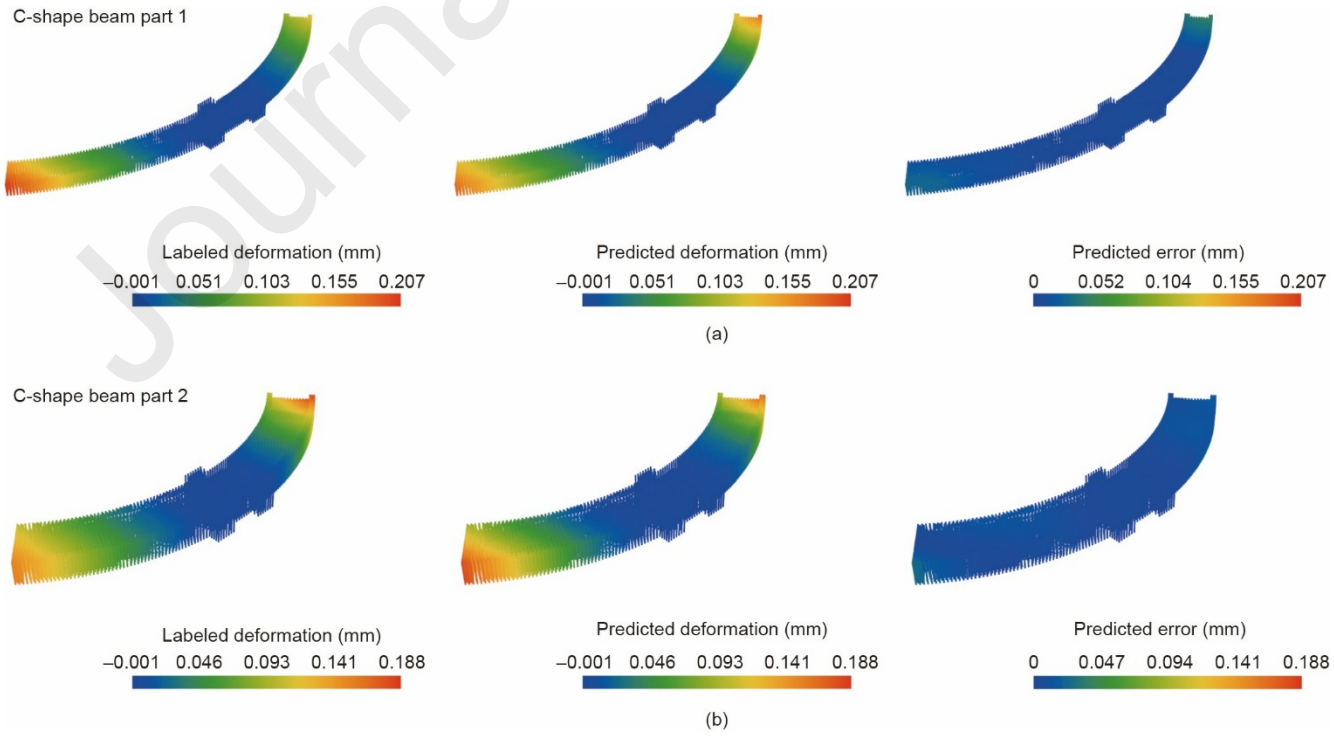

Fig. 10. Predicted deformation results for two different C-shaped beam parts under varying stress fields and geometries. (a) C-shape beam part 1: comparison of labeled deformation, predicted deformation, and predicted error. (b) C-shape beam part 2: comparison of labeled deformation, predicted deformation, and predicted error.

Fig. 11 provides data for a more comprehensive evaluation of the model performance by showing the error distributions for all parts of the test datasets. Figs. 11(a) and (c) compare the labeled and predicted deformation values for 10 different parts in the frame and C-shaped beam test datasets, respectively. We randomly sampled 2000 points from each part's deformation field. The diagrams reveal a strong correlation between the predicted and labeled values, as most points are aligned close to the zero-error line. Moreover, all the points are concentrated within the ±0.05 mm error range, indicating that the model's predictions met the accuracy requirements for practical machining applications.

Further analysis of the prediction errors for all the parts is presented in Figs. 11(b) and (d). The error distribution plots for the frame and C-shaped beam components indicate that the prediction errors are generally centered around zero. However, there were some variations in the error spread, with a slight divergence observed in certain parts. This variability may be due to the warping deformation characteristics of these structures, where deformation tends to be more pronounced at specific locations, such as at the ends. Despite these minor divergences, the majority of the predictions remain well within ±0.05 mm. The violin plots show that the errors were relatively evenly distributed across the different parts, proving the robustness of the model in maintaining accurate predictions across diverse geometries and conditions. This further proves the ability of the model to be effectively generalized under different machining scenarios.

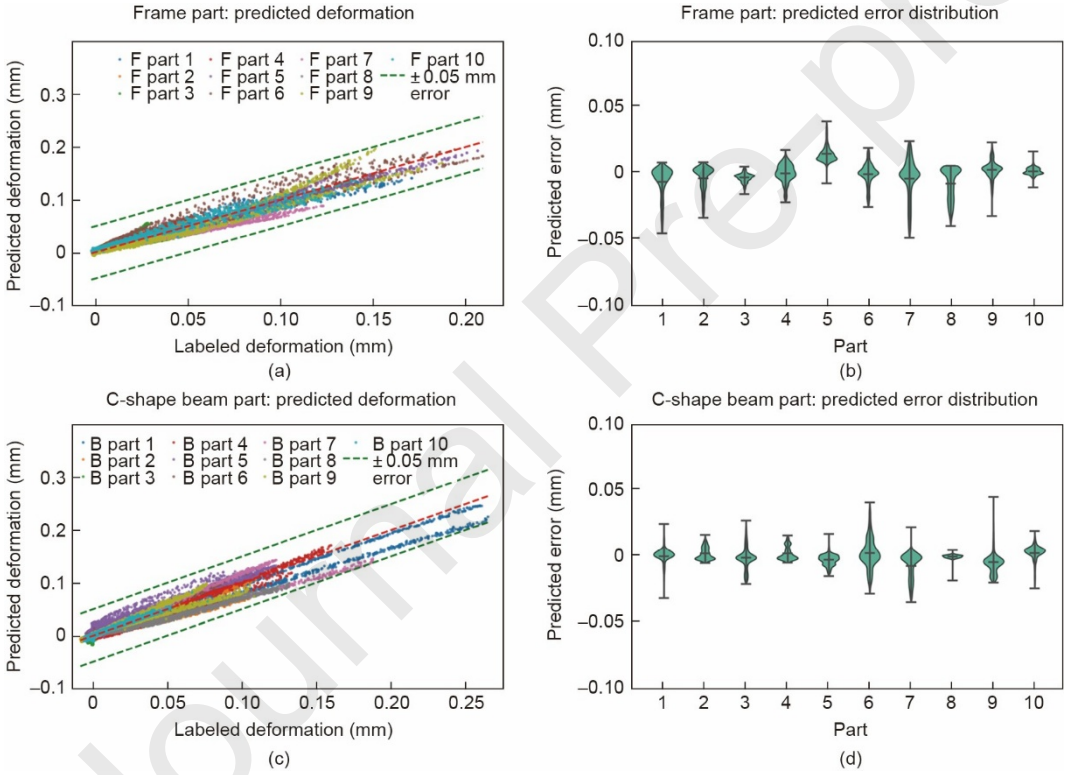

Fig. 11. Comparison of predicted versus label deformations and error distributions along the length direction for frame and C-shaped beam parts test sets. (a) Comparison of predicted and labeled deformation for frame parts along the length direction. (b) Error distribution of predicted deformation for frame parts. (c) Comparison of predicted and labeled deformation for C-shape beam parts along the length direction. (d) Error distribution of predicted deformation for C-shape beam parts.

To validate the effectiveness of the proposed GONO model and assess the impact of global geometric information embedding (GIE), we conducted a comparative analysis against GONO (without GIE) and the general neural operator transformer (GNOT) [26]. The comparison metrics included the root mean square error (RMSE) and mean absolute error (MAE) for both the frame and C-shaped beam parts, as shown in Fig. 12.

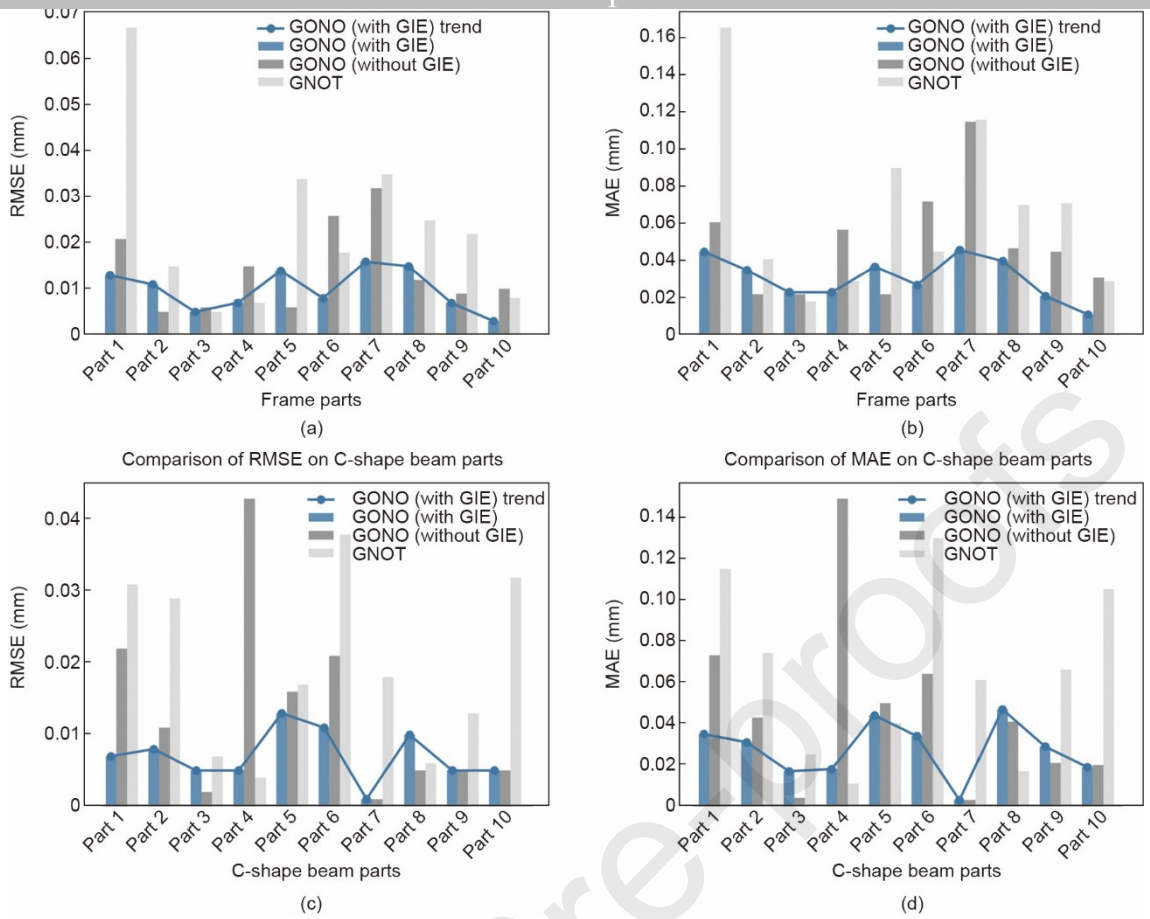

Fig. 12. Comparison of RMSE and MAE for different methods on frame and C-shaped beam parts. (a, b) show the RMSE and MAE comparison for different frame parts, respectively, whereas (c, d) present the corresponding RMSE and MAE results for C-shaped beam parts, respectively.

Compared to GONO without GIE, the GONO model with GIE exhibited more stable predictions, as indicated by the smoother RMSE and MAE variations across the different structural parts. The introduction of global geometric information enhances the model's ability to capture overall geometric constraints and improves generalization. Furthermore, the comparison results with GNOT indicated that GNOT exhibited higher error variability, with some structural components exhibiting significantly larger prediction deviations. In contrast, GONO with GIE maintained a more stable and narrower error range. This proves that the GIE mechanism effectively integrates the geometric constraints into the model, thereby enhancing its ability to generalize across different structural components. Additionally, the GONO model with GIE achieved lower RMSE and MAE values than GNOT for most of the frame and C-shaped beam parts, demonstrating better prediction accuracy. For the proposed GONO model, the RMSE values for both the frame and C-shaped beam parts remained consistently low, ranging from 0.001 to 0.016 mm, with maximum prediction errors between 0.003 and 0.047 mm. These error margins were well within the acceptable limits for most practical machining applications, proving the ability of the model to provide accurate deformation predictions. More prediction results for other types of components are provided in Supplement S2 in Appendix A.

3.2.3. Optimization of machining position for deformation control using GONO prediction model

To further evaluate the applicability of the proposed model in machining process optimization, it was used to minimize machining-induced deformation by optimizing the machining position. The residual-stress distribution within a workpiece varies depending on its position relative to the raw material, which directly affects the final deformation. Deformation can be effectively controlled by selecting an optimal machining position. As an example, a 600 mm × 120 mm × 24 mm component with an initial blank thickness of 40 mm was analyzed. The machining position varied along the depth direction in 1 mm increments, resulting in 17 possible positions, each requiring a deformation prediction. The proposed model completed 17 predictions in 3.69 s, whereas the FEM required 31 min for the same task.

The deformation prediction results for different machining positions are shown in Fig. 13. The results show that when the machining position is set at a depth of 9 mm, the predicted deformation remains within the −0.020 to 0.012 mm range, demonstrating effective deformation control. A comparison with FEM proved that the proposed GONO model

provided accurate and computationally efficient deformation predictions, enabling real-time machining process

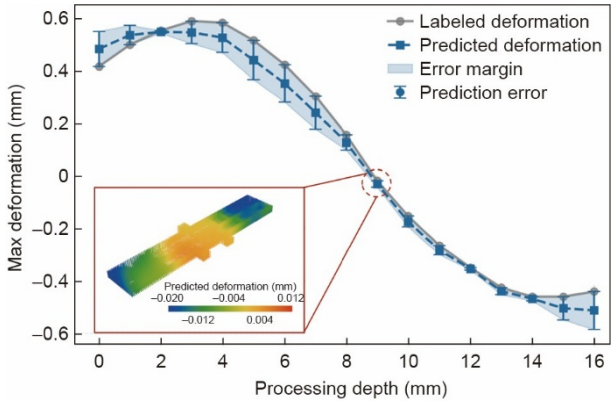

Fig. 13. Comparison of predicted and FEM deformation results for different machining positions, showing the variation of maximum deformation with machining depth and indicating that the optimal machining position at 9 mm depth minimized deformation within −0.020 to 0.012 mm.

3.2.4. Computational efficiency and sampling robustness

To further demonstrate the practicality of the proposed model, a comparison with the finite element simulation results was conducted in terms of computational time (Fig. 14). In terms of computational efficiency, the proposed model dramatically reduces the computational time by three orders of magnitude compared with the FEM. The FEM simulation times ranged from 46 to 92 s, whereas the prediction times for the proposed model were between 0.012 s and 0.094 s. This indicates that the proposed model exhibits a significantly lower computation time while maintaining a high prediction accuracy compared to the FEM. This significant reduction in computational time proves the suitability of the model for real-time or near-real-time applications in machining processes, where rapid and accurate deformation predictions are essential.

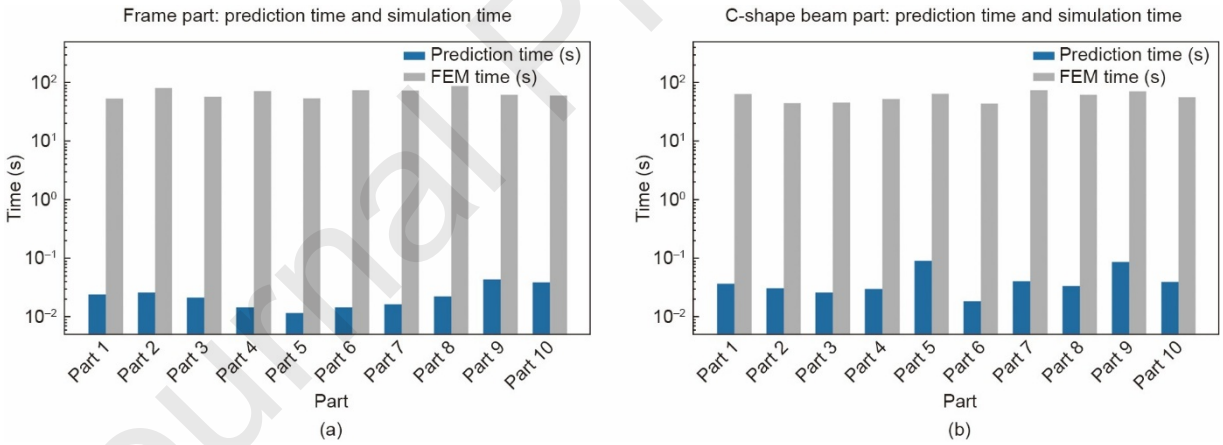

Fig. 14. Comparison of computational time of FEM and proposed method. (a) Computational time for frame parts. (b) Computational time for frame parts C-shape beam.

Additionally, the proposed model demonstrated the capability of accurately predicting the deformation fields across varying sampling densities, as shown in Fig. 15. Figs. 15(a) and (b) illustrate the RMSE for the frame and beam test sets at different sampling levels ranging from $2^1 \times 10^3$ to $2^6 \times 10^3$ points. The results indicated that the model maintained a consistent prediction accuracy across sampling densities. This consistency proved that the model exhibited discretization invariance. This adaptability ensures that the model can be effectively applied in various practical applications under different sampling conditions.

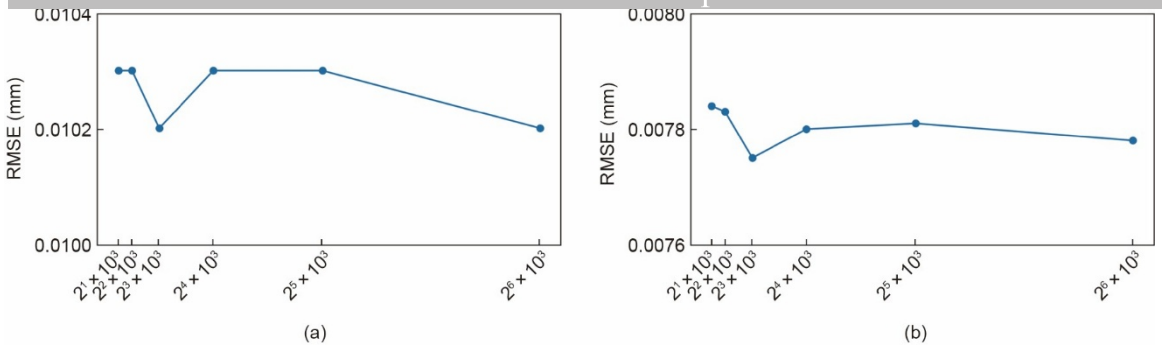

Fig. 15. RMSE of the predicted deformation fields across different sampling densities for (a) frame parts and (b) beam parts.

4. Discussion

The proposed GONO demonstrates strong generalization across varying geometries and stress fields without the need for retraining. In the experiments, GONO achieved high accuracy and computational efficiency in predicting the deformation fields of the tested structural components, including rectangular frames and C-shaped beams, which have the potential to be extended to other structures when additional datasets are available. The model consistently demonstrated a low RMSE and minimal MAE across various geometries and stress fields, effectively generalizing to different scenarios. The robustness of the model to varying sampling densities further proved its discretization invariance, allowing it to adapt to different input and output resolutions in practical settings. Compared with conventional FEM methods, GONO achieves similar prediction accuracy with computation speeds up to three orders of magnitude faster. In contrast to PINNs and existing neural operators, which are typically restricted to fixed domains or require retraining, GONO integrates global geometric information, enabling efficient and flexible deformation field prediction for diverse structural components.

Despite its effectiveness, minor prediction errors were observed at component ends due to localized warping. These limitations suggest potential for further improvement by incorporating local refinement or physics-informed constraints. Overall, GONO shows promise for real-time deformation prediction in intelligent manufacturing.

5. Conclusions and further work

In this study, a general model (GONO) for predicting deformation fields in components with varying geometries and stress fields was developed and tested. Unlike conventional methods, which often require retraining or development of new models when the geometry or stress fields change, GONO is flexible and adaptable across a wide range of scenarios where fast prediction and decision-making are required. Future research should extend this foundational model to include broader scenarios. First, the framework can be adapted to more complex structural components, including curved surfaces and structures. Second, the model can be expanded to handle dynamic stress fields that evolve during machining, enabling it to replace the FEM for simulating machining sequences and process-dependent stress variations. Furthermore, integrating physics-informed constraints into the neural operator framework can enhance the model interpretability, prediction accuracy, and generalization ability across diverse machining conditions.

Acknowledgements

This study was funded by the National Natural Science Foundation of China (grant no. 52175467) funded by Changqing Liu, the National Science Fund of China for Distinguished Young Scholars (grant no. 51925505) funded by Yingguang Li, and the Engineering and Physical Sciences Research Council (grant no. EP/V007335/1, “RIED: Re-Imagining Engineering Design”) led by Mark Price and Yan Jin.

Compliance with ethics guidelines

Zhiwei Zhao, Changqing Liu, Yan Jin, Yifan Zhang, and Yingguang Li declare that they have no conflicts of interest or financial conflicts to disclose.

References

[1] Zoch HW. Distortion engineering: vision or ready to application? Materialwiss Werkstofftech 2009;40(5-6):342–8.

[2] Aurrekoetxea M, Llanos I, Zelaieta O, López de Lacalle LN. Towards advanced prediction and control of machining distortion: a comprehensive review. Int J Adv Manuf Technol 2022;122(7-8):2823–48.

[3] Akhtar W, Lazoglu I, Liang SY. Prediction and control of residual stress-based distortions in the machining of aerospace parts: a

[4] Zhao Z, Liu C, Li Y, Gao J. A new method for inferencing and representing a workpiece residual stress field using monitored deformation force data. Engineering 2023;22:49–59.

[5] Zhang Z, Zhang Z, Zhang D, Luo M. Milling distortion prediction for thin-walled component based on the average MIRS in specimen machining. Int J Adv Manuf Technol 2020;111(11-12):3379–92.

[6] Hussain A, Lazoglu I. Distortion in milling of structural parts. CIRP Ann 2019;68(1):105–8.

[7] Prete AD, Franchi R, Antermite F, Donatiello I. Numerical simulation of machining distortions on a forged aerospace component following a one and a multi-step approaches. AIP Conf Proc 2018;1960(1):070009.

[8] D'Alvise L, Chantzis D, Schoinochoritis B, Salonitis K. Modelling of part distortion due to residual stresses relaxation: an aerOnautical case study. Procedia CIRP 2015;31:447–52.

[9] Cerutti X, Mocellin K. Parallel finite element tool to predict distortion induced by initial residual stresses during machining of aeronautical parts. Int J Mater Form 2015;8(2):255–68.

[10] Ma K, Goetz R, Srivatsa SK. Modeling of residual stress and machining distortion in aerospace components. In: Furrer DU, Semiatin SL, editors. Metals Process Simulation. 22B. Materials Park: ASM International; 2010. p. 386–407.

[11] Raissi M, Perdikaris P, Karniadakis GE. Physics-informed neural networks: a deep learning framework for solving forward and inverse problems involving nonlinear partial differential equations. J Comput Phys 2019;378:686–707.

[12] Kovachki N, Li Z, Liu B, Azizzadenesheli K, Bhattacharya K, Stuart A, et al. Neural operator: learning maps between function spaces with applications to PDEs. J Mach Learn Res 2023;24(1):4061–57.

[13] Liu G, Zhao Z, Fu Y, Xu J, Li Z. Deformation analysis and error prediction in machining of thin-walled honeycomb-core sandwich structural parts. Int J Adv Manuf Technol 2018;95(9-12):3875–86.

[14] Rodríguez-Sánchez AE, Ledesma-Orozco E, Ledesma S. Part distortion optimization of aluminum-based aircraft structures using finite element modeling and artificial neural networks. CIRP J Manuf Sci Technol 2020;31:595–606.

[15] Zhao Z, Li Y, Liu C, Gao J. On-line part deformation prediction based on deep learning. J Intell Manuf 2020;31(3):561–74.

[16] Zhao Z, Li Y, Liu C, Chen Z, Chen J, Wang L. A subsequent-machining-deformation prediction method based on the latent field estimation using deformation force. J Manuf Syst 2022;63:224–37.

[17] Azizzadenesheli K, Kovachki N, Li Z, Liu-Schiaffini M, Kossaifi J, Anandkumar A. Neural operators for accelerating scientific simulations and design. Nat Rev Phys 2024;6(5):320–8.

[18] Lu L, Jin P, Pang G, Zhang Z, Karniadakis GE. Learning nonlinear operators via DeepONet based on the universal approximation theorem of operators. Nat Mach Intell 2021;3(3):218–29.

[19] Li Z, Kovachki NB, Azizzadenesheli K, Liu B, Bhattacharya K, Stuart A, et al. Fourier neural operator for parametric partial differential equations. In: Proceedings of the International Conference on Learning Representations

(ICLR 2021); 2021 May 3–7; Virtual Event, Austria. Ithaca: OpenReview.net; 2021. p. 1–16.

[20] Huang P, Leng Y, Lian C, Liu H. Porous-DeepONet: learning the solution operators of parametric reactive transport equations in porous media. Engineering 2024;39:94–103.

[21] Jin P, Meng S, Lu L. MIONet: learning multiple-input operators via tensor product. SIAM J Sci Comput 2022;44(6):A3490–514.

[22] Yin M, Zhang E, Yu Y, Karniadakis GE. Interfacing finite elements with deep neural operators for fast multiscale modeling of mechanics problems. Comput Methods Appl Mech Eng 2022;402:115027.

[23] Chen G, Liu X, Meng Q, Chen L, Liu C, Li Y. Learning neural operators on riemannian manifolds. Natl Sci Open 2024;6(3):20240001.

[24] He J, Koric S, Abueidda D, Najafi A, Jasiuk I. Geom-DeepONet: a point-cloud-based deep operator network for field predictions on 3D parameterized geometries. Comput Methods Appl Mech Eng 2024;429:117130.

Proceedings of the 37th International Conference on Neural Information Processing Systems; 2023 Dec 10–16; New Orleans, LA, USA. New York City: Curran Associates Inc.; 2023. p. 35836–54.

[26] Hao Z, Wang Z, Su H, Ying C, Dong Y, Liu S, et al. GNOT: a general neural operator transformer for operator learning. In: Proceedings of the 40th International Conference on Machine Learning; 2023 Jul 23–29; Honolulu, HI, USA. New York city: PMLR; 2023. p. 12556–69.

[27] Li Z, Huang DZ, Liu B, Anandkumar A. Fourier neural operator with learned deformations for PDEs on general geometries 2023;24(1):18539–618.

[28] Yin M, Charon N, Brody R, Lu L, Trayanova N, Maggioni M. DIMON: learning solution operators of partial differential equations on a diffeomorphic family of domains. 2024. arXiv:2402.07250v1.

[29] Zhao Z, Liu C, Li Y, Chen Z, Liu X. Diffeomorphism neural operator for various domains and parameters of partial differential equations. 2025;8:15.

Declaration of Interest Statement

☒ The authors declare that they have no known competing financial interests or personal relationships that could have appeared to influence the work reported in this paper.

☐ The author is an Editorial Board Member/Editor-in-Chief/Associate Editor/Guest Editor for this journal and was not involved in the editorial review or the decision to publish this article.

☐ The authors declare the following financial interests/personal relationships which may be considered as potential competing interests: